Available online at www.sciencedirect.com
SCIENCE DIRECT®
Journal of Solid State Chemistry 173 (2003) 172–188
JOURNAL OF SOLID STATE CHEMISTRY
http://elsevier.com/locate/jssc

Interfacial chemistry in internally oxidized (Cu,Mg)-alloys

M. Backhaus-Ricoult,[a,*] L. Samet,[b,c] M.-F. Trichet,[a] M. J. Hÿtch,[a] and D. Imhoff[b]

[a] *Centre d'Etudes de Chimie Métallurgique, CNRS, 15 rue G. Urbain, 94407 Vitry sur Seine, France*
[b] *Laboratoire de Physique des Solides, CNRS, Bat 510, Université Paris-Sud, 91405 Orsay, France*
[c] *Laboratoire Physique de la Matière Condensée, Faculté des Sciences, 1060 Tunis, Tunisia*

Received 7 June 2002; received in revised form 3 October 2002; accepted 28 October 2002

Abstract

(Cu,Mg) alloys are internally oxidized at different oxygen chemical potential at 900°C. Oxidation scale microstructure is studied by SEM and TEM. MgO forms as large magnesia agglomerates without any special orientation relationship and isolated cubo-octahedral topotaxial MgO precipitates, the shape of which varies with decreasing oxygen activity from octahedral to cubic. The interfaces of the cubo-octahedral precipitates are studied in detail by CTEM, HREM and EELS. At the highest oxygen activity, important rigid-body contraction/expansion across the interface is found together with a strong modification in the interfacial electronic structure (compared to the adjacent bulk phases) indicating important hybridization of O 2*p* and Cu 3*d* states. Both suggest oxide bonding. At lower oxygen activity, interfaces show increasing structural disorder in the copper phase and microfaceting or terracing of the interfacial plane; the intensity of interfacial ELNES features associated to the O 2*p* and Cu 3*d* hybridization diminishes and finally disappears with decreasing oxygen activity. Changes with oxygen chemical potential in precipitate morphology, interface atomic and electronic structure are explained by Gibbs' adsorption/desorption of excess oxygen to the interface. Adsorption isotherms are modeled for various configurations and compared to the experimental results.

Keywords: Internal oxidation; Interface; TEM; ELNES; MgO; Cu

1. Introduction

Structure and chemistry of metal–oxide interfaces are of crucial importance for mechanical, electronic and magnetic properties of components such as electronic devices, structural composites and memory storage systems. Even though the relation between properties and microstructure can often be understood after a precise analysis of the local chemical composition and the chemical bonding across the interface, upon processing, the exact control of structure and chemistry at an interface still remains challenging. This is mainly due to an insufficient comprehension of kinetic and thermodynamic factors controlling interface formation in multicomponent systems. The coexistence of metal and oxide phases is in general not invariant from a thermodynamic point of view (except for the "binary" case of a metal in contact with its own oxide), and non-reactive metal–oxide interfaces are thermodynamically stable in a wide range of oxygen activity [1–4]. According to the extended Gibbs' phase rule, for fixed interface geometry, temperature and pressure, interfaces in such ternary systems are uni-variant and vary with the oxygen chemical potential. Within the entire stability range, the interface constitutes the boundary between the same two bulk phases, but their chemical component potentials change over orders of magnitude. While the chemical compositions of the bulk phases often remain almost unaffected (see coexisting bulk MgO and bulk Cu), local interfacial composition may vary much more.

Systematic studies on the influence of the oxygen chemical potential on metal–oxide interfaces revealed changes in interfacial bonding for several different systems. For Ag–MgO interfaces, adsorption of excess oxygen with increasing oxygen partial pressure was followed by titration [5]. For Cu–MgO [6–9], Cu–SiO_2 [10] Ag–MgO [11] and Cu–Al_2O_3 [12] interfaces, systematic variations in interfacial electronic states with oxygen chemical potential were found. In the MgO–Cu

*Corresponding author. Department of Materials Science and Engineering, Cornell University, Ithaca, NY 14853, USA. Fax: +1 607-255-2365.
E-mail address: monika@ccmr.cornell.edu (M. Backhaus-Ricoult).

0022-4596/03/$ - see front matter © 2002 Elsevier Science (USA). All rights reserved.
doi:10.1016/S0022-4596(02)00127-5

system, changes in equilibrium shape with oxygen activity of small MgO precipitates in a copper matrix [13,14] and of small copper inclusions in MgO [15] were observed, demonstrating the dependency of the interfacial energy and the interfacial chemistry on the oxygen chemical potential. A similar dependency on oxygen activity was found for the wetting behavior of various oxides by liquid copper [16,17].

Ab initio calculations of metal–oxide interfaces at different oxygen chemical potential conducted by Batyrev et al. [18,19] predicted changes with oxygen chemical potential of the interfacial composition at alumina–Nb interfaces. Finnis' approach was also adopted in Ref. [20]. In general, it can be noted, that ab initio calculations in a grand-canonical system require very large computing capacities, and that in the present days, it is not yet possible to effectuate calculations with a systematic variation of interfacial plane, oxygen activity and temperature, and, in addition, for a large number of systems. In order to respond to this demand, the phenomenological model of Gibbs' adsorption was applied to metal–oxide interfaces by one of the authors [21,22]. It allows to evaluate the influence of crystallography and thermodynamic variables, oxygen chemical potential and temperature, but, of course, does not possess the precision in interaction parameters as ab inito calculations.

The aim of this work is to present experimental results on relative energy, chemical composition, atomic and electronic structure of MgO–Cu interfaces as a function of oxygen activity. The interfaces are produced by internal oxidation of (Cu,Mg) alloys. Internal oxidation of Cu-alloys was widely studied in the past [23–25], but the interfaces produced at different reaction conditions were not analyzed in detail. Some details on interfaces obtained at special reaction conditions were reported in [6,7,8,9,26,27]. In the present publication, we combine experimental results from those studies with new investigations, use more sensitive methods for extracting the interface-related information (phase imaging for HREM images and multivariate statistical analysis for ELNES data) and present the entity of the results obtained by different techniques. Then we interpret those results in terms of the interfacial chemistry and compare them to predictions made by the Gibbs' adsorption model [22].

2. Experimental procedures

2.1. Elaboration of different Mgo-Cu interfaces

(Cu,Mg) alloys were prepared by melting in levitation 99.999% pure copper (Johnson Matthey) and 99.8% grade magnesium (Pechiney) under a flow of purified argon inside a copper crucible. Single crystals were obtained by slowly driving (16 mm/h) under a flow of purified Argon the ingots in a conic carbon crucible through the hot zone of a Bridgeman furnace. The crystals were oriented in a Laue diffractometer and then cut into slices with (001) and (011) surfaces. SEM observations, X-ray diffraction and TEM analysis did not reveal any second phases and showed that the alloys were very homogeneous. Chemical analysis of the alloy ingots (by ICP) confirmed the absence of any pollution and provided the exact alloy compositions with 1.06, 2.04 and 2.97 at% magnesium.

Polished parallelepipeds of 3 mm × 3 mm × 4 mm were oxidized at 900°C for times between 10 and 1000 h (to reach equilibrium precipitate shape and establish equilibrium structure and chemistry at the interfaces) at different oxygen activities:

- a_{O_2} (Cu/Cu_2O/MgO) = $10^{-7.3}$
- $a_{O_2} = 10^{-11} - 10^{-15}$ (established by flow of buffering CO/CO_2 gas mixtures; the exact oxygen activity was measured at the furnace gas-inlet and -outlet by a zirconia oxygen sensor heated at 735°C).
- $a_{O_2} = 10^{-20}$ (C/CO buffer)
- a_{O_2} (Mg/MgO/Cu) = 10^{-38} at 1000°C (Internal oxidation cannot be used to directly produce MgO precipitates in Cu at the oxygen activity of coexisting (Cu,Mg/MgO), since the alloy is stable and no oxidation occurs. Therefore, MgO was first precipitated at 900°C and high oxygen activity and afterwards equilibrated at 1000°C, in a Mg/MgO/Cu buffer mixture. At this higher temperature, the magnesium solubility in the alloy is lower and precipitates do not redissolve.
- Thermal treatments were realized in a tubular furnace, the temperature of which was controlled with a Pt/PtRh10 thermocouple.

2.2. Characterization of the interfaces

Surfaces and polished cross-sections of oxidized samples were investigated by optical microscopy, analytical scanning electron microscopy (SEM/EDX) and X-ray diffraction. Prior to SEM investigations, samples were electrolytically polished (H_3PO_4, H_2O, C_2H_5OH and *n*-propanol mixture at 12°C under 15 V against a copper electrode).

Only samples oxidized for annealing times above 50 h were studied by TEM. For conventional, analytical, and high-resolution transmission electron microscopy (TEM) investigations, 3 mm diameter slices were mechanically polished to a thickness of 30 μm and ion-milled in a cold stage at 5 kV, 0.5 mA, at a 12° angle. For high-resolution TEM (HREM) and energy loss near edge fine structure (ELNES) investigations, extremely thin foils were prepared, which were cleaned by ion

milling from any traces of surface oxidation and pollution prior to each investigation.

Thin foils were investigated in a conventional transmission electron microscope (CTEM JEOL 2000 FX). The different types of precipitates were identified and characterized by their orientation relationship with the matrix, their morphology and their interfacial facets.

The interfaces of the small, regularly shaped cubo-octahedral precipitates were studied in more detail by HREM and EELS. HREM analysis was performed on a TOPCON 002B microscope (200 kV, Cs = 0.4 mm). Images were taken close to the Scherzer focus. Bragg-filtered images and geometric phase images were used to reveal local lattice perturbations, to identify the position of the interface and locate interfacial dislocations [28]. The latter method consists of selecting individual lattice fringes by means of masks (in our case Gaussian shaped) in Fourier space. The resulting phase images are directly related to the displacement of the lattice fringes, and hence the local lattice spacing and orientation. The position of the interface between MgO and Cu was determined from maps of the local lattice spacing. The occupancy of the final magnesia interfacial plane was deduced from the interplanar distance across the interface measured by the geometric phase images.

Electron energy loss spectroscopy (EELS) analysis was realized on a VG HB 501 dedicated scanning transmission electron microscope (STEM), operated at 100 kV with a field emission gun and equipped with a GATAN parallel EELS spectrometer. The inclination of the interfacial plane with respect to the beam was controlled by High Angle Annular Dark Field (HAADF) imaging and was kept smaller than 2–3°. Spectra were acquired at the interfaces of the cubo-octahedral precipitates, in bulk MgO and Cu and for reference materials Cu_2O, CuO and mixed (Cu,Mg) alloys.

Spectra were acquired using photodiode arrays during 25–300 ms for the low loss region (zero loss, plasmon region, Mg-2*p* and Cu-3*p* edges) and for 2-5 *s* for the O-1 *s* and Cu-2*p* core edges, respectively. The amplification of the present set-up was insufficient to acquire the Mg-1 *s* edge at 1305 eV. Probe size of 0.7 nm, spectrometer collection semi-angle of 16 mrad and energy dispersion of 0.2 eV/ch or 0.5 eV/ch were used for the study. Continuously monitoring the time-evolution of the spectra helped to optimize the acquisition conditions (time and beam current) and avoid any modification of the interfacial bonding by irradiation. Series of 32 to 64×1 to 8 spectra were acquired as image spectrum [29] with the scanned line being perpendicular or parallel to the interface. The probe displacement between successively acquired spectra was 0.6 nm.

Direct comparison of spectra recorded within matrix or precipitate phase with interfacial spectra reveals qualitative differences. However, smallest differences between interfacial region and bulk were extracted by a Normalized Spatial Difference (NSD) approach. In this method, normalized bulk, interface and reference spectra are formed by scaling the spectral intensity in a selected energy interval. The NSD spectrum was then obtained by subtracting the matrix absorption edge (metallic copper or magnesia) from the corresponding interfacial spectrum. NSD spectra were compared to linear combinations of reference edges.

In general, it cannot be expected that bulk phases always provide suitable references for the interfacial states, because the break in symmetry at the interface and changes in the atomic distances may alter the ELNES features. However, if the fit is good, the comparison to reference bulk phases provides valuable insight.

The spectrum-image technique provides simultaneously information on energy loss and probe location. Multivariate Statistical Analysis [30,31] (MSA) was used to increase the signal-to-noise ratio and to detect and locate ELNES variations. MSA is a signal decomposition method, which analyses the variance of the complete set of data from every probe position and energy loss channel. MSA is most efficient for a large number of spectra, but shows already a significant improvement in the signal-to-noise ratio for 32 spectra.

Even for sample thickness below $t/\lambda < 0.5$ multiple scattering and non-adapted background subtraction may raise problems, therefore, spectra were deconvoluted from multiple scattering using an approach developed in Ref. [32]. After deconvolution, the background was fitted by a power law and subtracted.

3. Experimental results and interpretation

3.1. Oxidation scale microstructure

3.1.1. Influence of the relative size of magnesium and oxygen diffusion fluxes on the scale microstructure

Upon oxidation of the alloys at all different oxidation conditions, MgO formed as internal oxidation product. While at high oxygen activity and low magnesium content, precipitates were isolated, extremely small in size and clearly facetted, at lower oxygen activity and higher initial magnesium content, larger, irregularly shaped magnesia agglomerates formed in proximity of the outer surface, see Fig. 1. These agglomerates grew with reaction time and eventually formed a continuous layer, which then inhibited further oxidation.

According to Wagner's theory of alloy oxidation [4], oxidation may occur by in-diffusion of oxygen into the alloy or by out-diffusion of magnesium, leading then to inner and outer oxidation scales, respectively. Internal oxidation occurs if the transport product of oxygen is

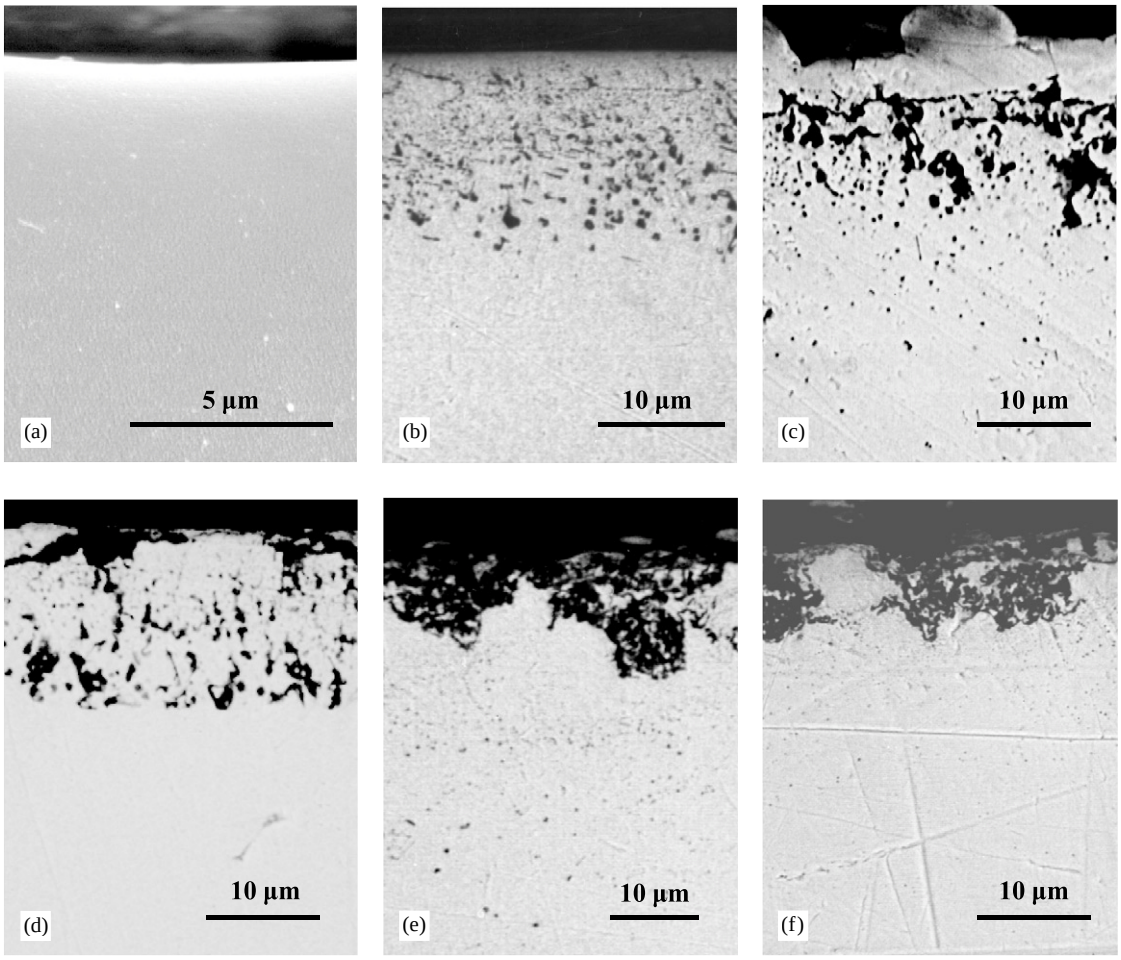

Fig. 1. Polished cross sections of oxidized (Cu,Mg) alloys illustrating the increasing agglomeration of precipitated magnesia with decreasing oxygen activity and with increasing magnesium content in the alloy: (a) (Cu, 1%Mg), $a_{O_2} = 10^{-8}$, (b) (Cu, 1%Mg), $a_{O_2} = 10^{-13}$, (c) (Cu, 1%Mg), $a_{O_2} = 10^{-15}$, (d) (Cu, 2%Mg), $a_{O_2} = 10^{-15}$, (e) (Cu, 3%Mg), $a_{O_2} = 10^{-13}$, (f) (Cu, 3%Mg), $a_{O_2} = 10^{-15}$; $T = 900°C$, $t = 50$ h

larger than that of magnesium [4]: $D_O \cdot c_O \gg D_{Mg} \cdot c_{Mg}$. The magnesium contents in the studied alloys and the dissolved oxygen content at the studied reaction conditions fulfill this criterium. Effectively, for very short reaction times, always internal oxidation was observed. Precipitates were small in size and regularly distributed with volume fractions of precipitated MgO corresponding everywhere to that of the initial Mg alloy content. For longer reaction times, large MgO agglomerates were observed to form in addition to the small precipitates. They were located in a band at a certain distance under the outer sample surface, see Fig. 1. Agglomerate densities increased with increasing magnesium content in the initial alloy, with decreasing outer oxygen partial pressure and with oxidation time. In extreme cases, a continuous, dense magnesia layer formed in the depth of the sample and blocked completely any further progress of oxidation.

The reason for this can be found in a non-negligible magnesium flux compared to the oxygen flux. For long reaction times, oxygen potential gradient across the scale progressively diminishes with increasing scale thickness, while the magnesium concentration gradient in the alloy at the oxidation front does not considerably change. As a consequence, the contribution of the magnesium diffusion flux to the magnesia formation increases more and more with time and the local volume fraction of magnesia at the oxidation front is increased. We observed effectively magnesia fractal agglomerates, which formed at a certain depth in the scale. Their concentration and size increased with the magnesium alloy content and decreased with the applied chemical potential.

Differences in the oxide formation mechanism must be the cause for forming either fractal agglomerates or topotaxial facetted precipitates. The (simplified) thermodynamic condition for MgO phase formation is given by the solubility product $a_{Mg} \cdot a_O = \exp(-\Delta G^f(MgO)/RT)$ with a_i being the activity of i, $\Delta G^f(MgO)$ the Gibbs formation energy of MgO, R the gas constant and T the temperature (solubility of copper in the oxide is

neglected). This equation implies, that magnesia phase also forms for ratios of $Mg/O \neq 1$.

When the local oxygen content was low, it can be imagined that a magnesium-rich precursor formed, which, in a first stage, was coherent with the copper lattice and, only upon further indiffusion of oxygen, turned into incoherent stoichiometric MgO. Such a coherent precursor could grow in any morphology to large sizes and preserve its irregular shape upon transformation into incoherent MgO. Large size, irregularly shaped incoherent MgO particles would then need extremely long times and high activation energies to reach thermodynamic equilibrium shape by modifying their orientation and establishing low-energy faceting. For this reason, most of the large agglomerates we observed showed neither special shape, nor special orientation.

At high local oxygen content, initial coherent magnesia stable nuclei were oxygen-rich. Such nuclei strongly differed in bonding and structure from the metallic copper phase and, consequently, at a very early stage, formed an incoherent oxide with its proper crystal lattice and interface energetics. Controlled by magnesium medium range diffusion, small oxide particles then grew to larger size, respecting energy minimization upon their slow growth and yielding the topotaxial cubo-octahedra we observed.

3.1.2. *Influence of single-crystal orientation*

Comparison of the oxidation scales of alloy single crystals with different surface planes did not reveal any difference in the scale microstructure in the oxidation kinetics. The observation is understandable for the present fcc systems.

The influence of oxidation parameters, alloy composition and crystal orientation is summarized in Table 1.

3.2. *Characteristics of cubo-octahedral MgO precipitates*

3.2.1. *Morphology of precipitates within the alloy and at the alloy surface*

SEM observations of as-oxidized alloy surfaces and electrolytically polished samples revealed that the shape of precipitates at the alloy surface was very different from that adopted within the bulk alloy. Fig. 2a shows the as-oxidized (001) alloy surface of a sample after oxidation at 900°C, $a_{O_2} = 10^{-12}$ and Fig. 2b the same surface after electrolytical polishing. The as-oxidized alloy surface showed terracing of the copper metal with extended surface facets. It can be seen from Fig. 2a, that the MgO precipitates at the sample surface varied in shape, depending on their size and probably also (even though this is not visible in the image) on their penetration depth into copper. Common to most of the surface precipitates was that they all exhibited a large (001) surface facet, which strongly truncated the inclined octahedral facets.

Precipitates in the bulk, see Fig. 2b, did not have such large (001) surface facet; they showed very regular octahedral shape with minor (001) truncation. Fig. 2c shows the SEM view of an electrolytically polished (011) section. From this image and the corresponding TEM

Table 1
Systematic evolution of oxidation scale characteristics with oxidation and alloy parameters

	Small	Large
Oxygen chemical potential	Tendency to form a dense layer of large agglomerated MgO	Tendency to form uniformally distributed small topotaxial precipitates
Mg-content in alloy	Tendency to form uniformally distributed small topotaxial precipitates	Tendency to form a dense layer of large agglomerated MgO
Oxidation time	Nucleation and growth stage with kinetically controlled precipitate shape and non-equilibrium interface chemistry	Thermodynamic equilibrium with equilibrium precipitate shape and equilibrium interface chemistry
Oxidation temperature	Tendency for internal oxidation	Tendency for external oxidation
Size of agglomerated MgO precipitates close to the surface	— (does not occur)	Irregular shape of fractal agglomerates, interfacial chemistry was not studied
Size of topotaxial MgO precipitate	20-500 nm. No influence on precipitate shape and no influence on the equilibrium interfacial chemistry	—(does not occur)
Single-crystal orientation	No dependency on surface orientation	
Grain boundaries in polycrystals	Grain boundaries acted as internal surfaces	

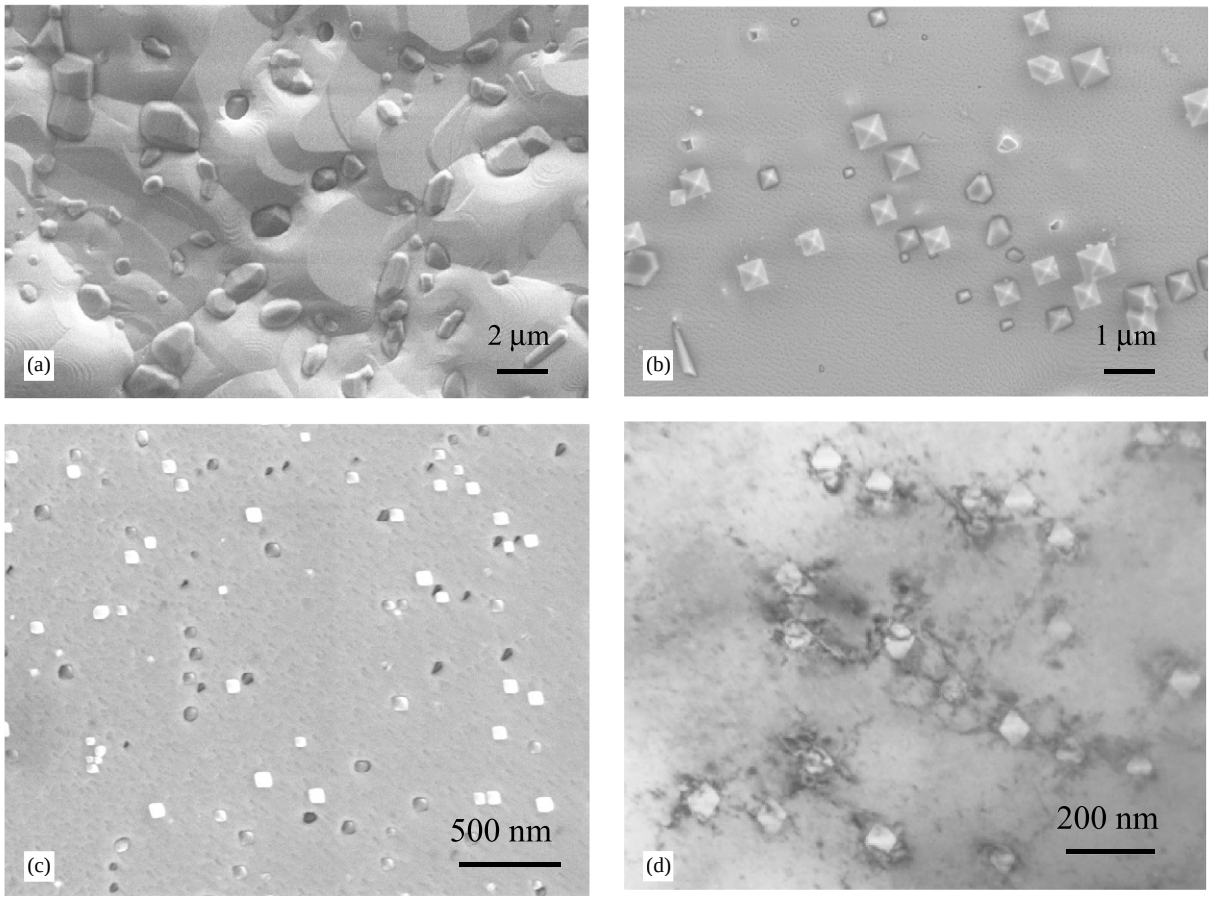

Fig. 2. (Cu1%Mg) alloy oxidized at 900°C, $a_{O_2} = 10^{-13}$. (a) SEM view of the as-oxidized (001) surface with magnesia precipitates with extended (001) facets. (b) SEM view of an electropolished (001) section below the outer surface revealing bulk precipitates with octahedral faceting. (c) SEM view of an electropolished (011) cross section revealing the cubo-octahedral precipitate shape. (d) TEM bright field image in [011] projection with selected area diffraction pattern of matrix and precipitates showing the topotaxial orientation of the octahedral MgO precipitates.

image of the same orientation in Fig. 2d, the precipitate shape with large {111} and small {001} facets can better be appreciated.

Morphology differences between bulk and surface precipitates have to be related to differences in the surface (MgO–gas) and interface (MgO–Cu) energies of magnesia. Effectively, for MgO, it is well known that {001} surfaces have by far the lowest surface energy. Calculations have shown that {111} surfaces have higher energy and decompose under faceting in {001} surfaces [35]. Our prior TEM observations suggested that $\{111\}_{MgO}///\{111\}_{Cu}$ were the lowest energy interfaces between copper and MgO at $a_{O_2} = 10^{-8}$, 900°C.

3.2.2. Dependency of precipitate morphology on size

At given oxygen chemical potential, the morphology of cubo-octahedral precipitates of different size was investigated for a large number of precipitates. Within the size range of 50–500 nm, no change in morphology was found. For precipitates with sizes around 20 nm and smaller, a small systematic evolution in shape was observed, which was related to the increasing contribution of edge and corner energies to the global interfacial energy of the precipitates. Precipitates above micrometer size showed deviation from the constant shape, because they were so large that they probably had not reached their equilibrium shape in the oxidation time. Based on this finding, we focussed our study on precipitates the size range from 100 to 200 nm.

3.2.3. Dependency of precipitate morphology on oxygen chemical potential

A comparison of electrolytically polished sections of samples oxidized at different oxygen chemical potential revealed an important evolution of the morphology of the cubo-octahedral precipitates with oxygen chemical potential. Fig. 3 presents SEM images of electrolytically polished $(011)_{Cu}$ surfaces of alloys oxidized for 50 h at 900°C and different oxygen activities. EDX analysis confirmed that all precipitates were MgO. Differences in image contrast are due to different charging states of the precipitates. MgO is an isolator, therefore, precipitates,

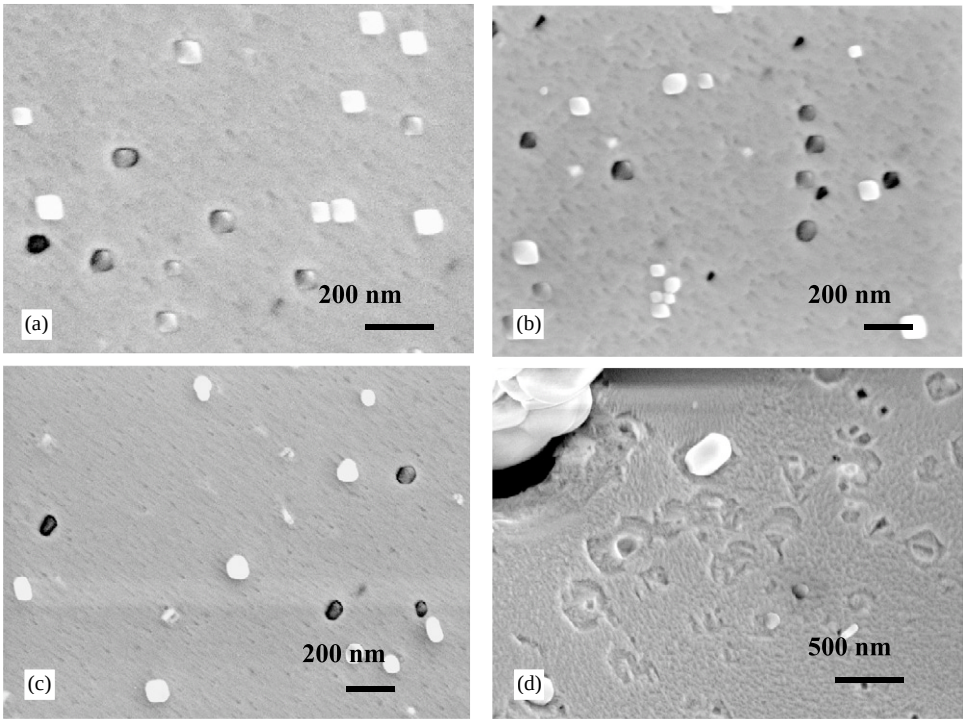

Fig. 3. SEM/FEG images of electrolytically etched oxidized (Cu 1%Mg) alloy, showing the shape evolution of MgO precipitates formed at $T=900°C$ at oxygen activity (a) $10^{-7.3}$, (b) 10^{-13}, (c) 10^{-15} and (d) 10^{-20}.

which were mostly embedded in copper, charged less and showed dark contrast in secondary electron SEM images. Precipitate shape appeared irregular, when the oxide was partly covered by copper. Precipitates, which largely exceeded the copper surface, suffered more charging and yielded white contrast.

Precipitates formed at $a_{O_2} = 10^{-73}$, Fig. 3a, had almost perfect octahedral shape. Truncation of the octahedron tips occurred while diminishing a_{O_2} and was more important the lower the a_{O_2}, Figures 3b,c. At $a_{O_2} = 10^{-20}$, isolated precipitates were scarce, however, Fig. 3d demonstrates that the {001} facet size was larger than the {111} facet size.

SEM imaging revealed a shape evolution, however, exact ratios of the facet sizes could not be deduced from these observations due to the non-uniformity in charge, partial coverage by copper and local variations in the etched surface plane.

TEM sample cross sections were used to quantify the morphology. Thin foils were oriented along the [001] and [011] directions of copper, revealing in the latter orientation the relative sizes of {111} and {001} facets by the ratio of the distances between parallel sets of facets. Electron diffraction revealed that precipitates were fcc MgO in topotaxial orientation with the copper matrix. The precipitate lattice parameter was that of bulk magnesia. An evolution in morphology was already reported in Ref. [13], the present results completed former findings, see Fig. 4. MgO precipitates were always limited by $\{111\}_{MgO}//\{111\}_{Cu}$ and $\{001\}_{MgO}//\{001\}_{Cu}$ facets. The relative facet size varied with oxygen activity, leading to formation of almost perfect octahedra at $a_{O_2} = 10^{-7}$, 900°C, of cubes at $a_{O_2} = 10^{-20}$, 900°C and of cubo-octahedra at intermediate values. Fig. 5 presents, for different oxygen activities, the TEM views of typical precipitates along the [011] directions, together with the corresponding reconstructed three-dimensional precipitate shape and its [011] projection.

At the lowest oxygen activity, $a_{O_2} = 10^{-31}$ at 1000°C, precipitates were found in many different orientations and also showed many different facets of low-index magnesia planes being parallel to high density copper planes. Since the reaction temperature used to produce the precipitates was higher, this result is not further included in our further considerations.

3.2.4. *Reversibility of changes in precipitate morphology*

By consecutively applying different oxidation conditions, it was shown that precipitates reversibly changed their morphology at 900°C. Precipitates formed at $a_{O_2} = 10^{-7}$ and then exposed to $a_{O_2} = 10^{-12}$ or 10^{-15} slowly changed their shape by increasing the {001} facet size upon the second annealing. While chemical and crystallographic phase limitations clearly indicated the modified morphology, defect arrays in the copper phase for {001} facets and in the magnesia phase for {111} facets, respectively, indicated some kind of memory of the original precipitate shape.

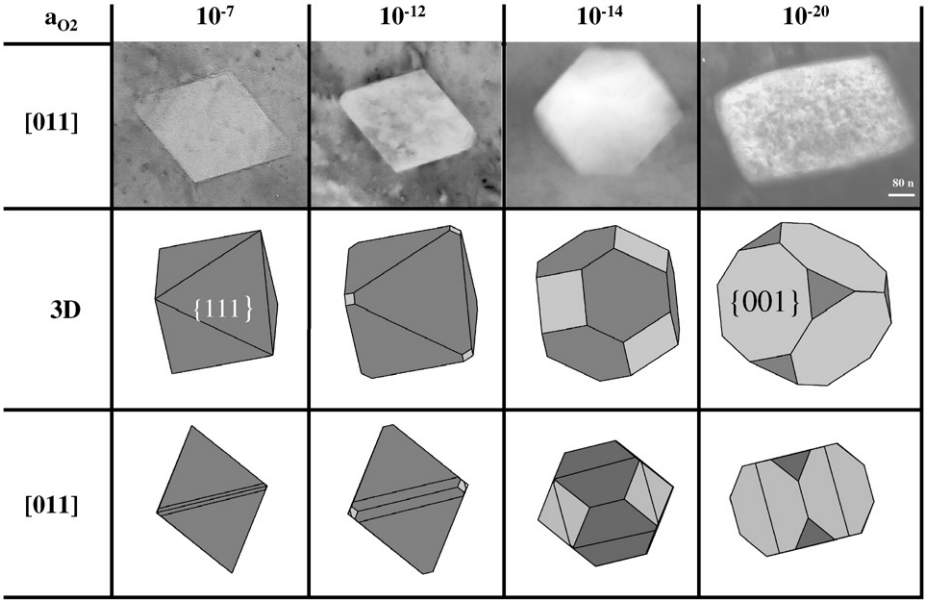

Fig. 4. TEM bright field [011] projections of topotaxial MgO precipitates within the copper matrix, precipitates were formed upon internal oxidation at 900°C at oxygen activities $a_{O_2} = 10^{-7.3}$, $10^{-12.3}$, $10^{-13.2}$ and 10^{-20}. The two additional columns in the table present the reconstructed three-dimensional precipitate shape and its projection along [011].

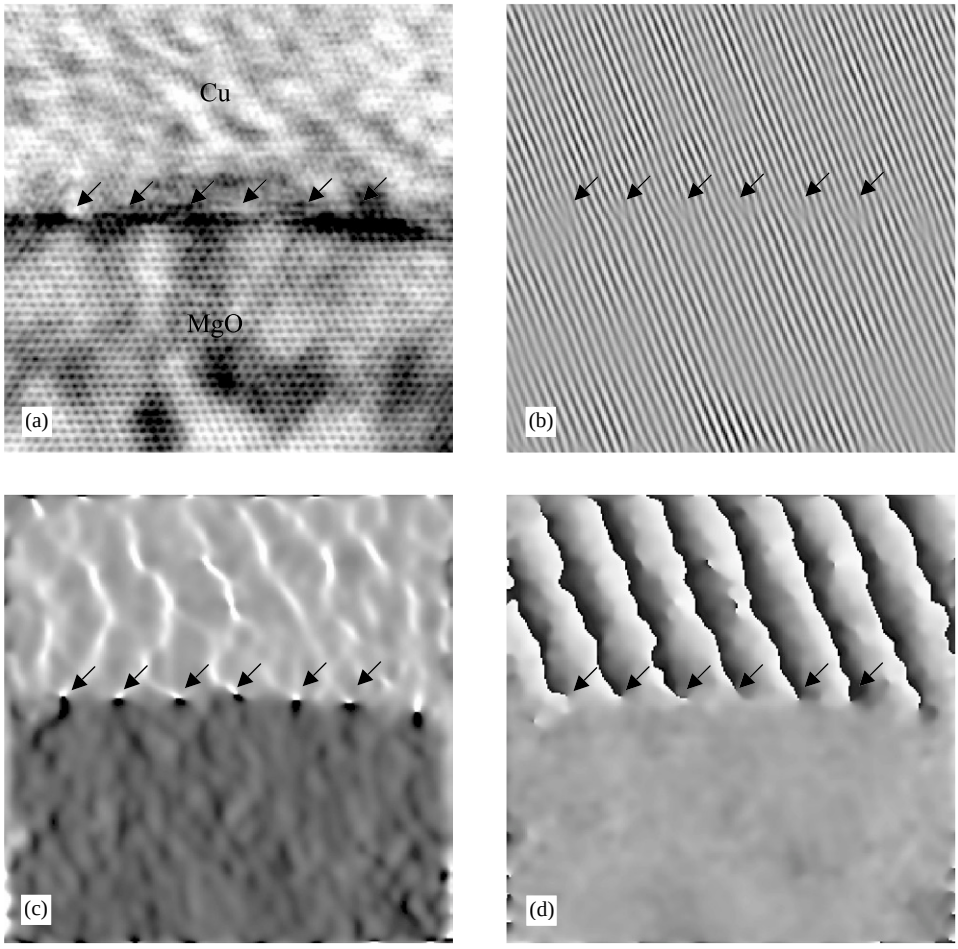

Fig. 5. (a) HREM images of the $(111)_{MgO}//(111)_{Cu}$ interfaces of a topotaxial MgO precipitate in Cu equilibrated at $a_{O_2} = 10^{-8}$ and 900°C, observation in [011] projection. (b) Corresponding Bragg filtered image for (111) lattice fringes. (c) Map of local reciprocal lattice vector (gray scale proportional to $g = 1/d_{111}$) and (d) Corresponding phase image (gray scale between 2 and 2π), arrows indicate the misfit dislocations.

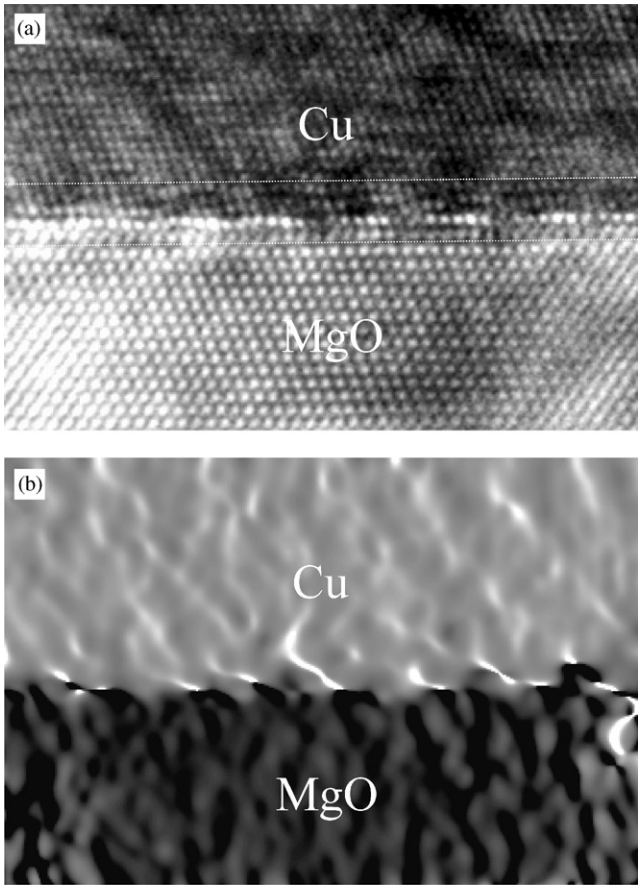

Fig. 6. (a) HREM images of the $(111)_{MgO}//(111)_{Cu}$ interface formed at 900°C, $a_{O_2} = 10^{-12}$ in [011] projection together with (b) the map of the local reciprocal lattice vector (gray scale proportional to $g = 1/d_{111}$).

3.3. Atomic structure of precipitate interfaces

For most oxidation conditions, $\{111\}_{MgO}//\{111\}_{Cu}$ and $\{001\}_{MgO}//\{001\}_{Cu}$ interfaces were formed. Both types of interfaces were flat over large areas, see Figs. 5–7. However, some limitations of interface processing by internal oxidation have to be mentioned. At the highest oxygen activity, $\{001\}_{MgO}//\{001\}_{Cu}$ facets were extremely small in size and, as a consequence, even for extremely thin foils, in the [011] orientation, these interfaces were covered by copper. At low oxygen activity, oxidation produced mainly irregular MgO agglomerates and outer scales; the density of topotaxial precipitates was low and restricted to surface-close areas. Therefore, it was difficult to find suitable precipitate facets.

According to lattice imaging, all MgO–Cu interfaces were semi-coherent, almost incoherent. The lattice mismatch of 14% between the two phases produced interfacial dislocations every seven planes in copper (six planes in MgO). This can be seen by the HREM image of the interface in Fig. 5a and more clearly by the Bragg-filtered image, Fig. 5b, and the phase image, Figs. 5d. The Bragg filtered image, Fig. 5b, shows the discontinuity of the planes at the interface and the additional planes on the copper side every seven planes. For phase imaging, the magnesia phase is taken as phase reference. As a consequence, the image shows a periodic phase shift for the copper phase. The discontinuities in phase correspond to the dislocation core positions [33]. While the magnesia lattice remained completely rigid, deformation in the metal extended over a few lattice planes on the copper side. At $a_{O_2} = 10^{-7.3}$, lattice deformations were limited to the first two copper lattice planes, interfacial strain being extremely localized at the interface and small in size, Figs. 5 and 7a. At intermediate oxygen activity, lattice strain fields extended to 3–4 lattice planes (Figs. 6 and 7b) and became even more delocalized and irregular at $a_{O_2} = 10^{-20}$ (Fig. 7c).

For polar $\{111\}_{MgO}//\{111\}_{Cu}$ interfaces, high-resolution image contrast was calculated by the multislice method for different occupancies of the MgO terminating plane: a fully occupied oxygen plane, a half-filled oxygen plane, and a completely filled magnesium plane. In our simple calculation, initial atom positions were fixed in continuity with the bulk lattice and not further relaxed. It was difficult to identify the type of terminating plane in the oxide by the comparison of experimental HREM images with simulated images due to the number of experimental parameters involved [6]. We therefore concentrated on the measurement of the rigid-body contraction/expansion across the interface, which is much less sensitive to experimental conditions, especially for centro-symmetric structures [34]. This experimentally measured distance across the interface can then be used as a qualitative characteristic parameter.

The measurement was carried out using the geometric phase images (see Fig. 5), the first step being the precise identification of the interfacial position. Fig. 5c shows the map of the local reciprocal lattice vector g for the (111) lattice fringes shown in Fig. 5b. The change in lattice spacing, given by transition from the dark to the light contrast, occurs at the interface between the two phases. This is corroborated by the misfit dislocations, which are also located in this plane (Fig. 5d). The phase change across the interface was then measured with respect to the terminating MgO (111) plane, giving directly the rigid-body displacement. The only remaining difficulty is that the contrast of the (111) lattice planes can be positive (located over atom plane positions) or negative (between planes), thus adding or subtracting half a (111) lattice spacing to the measured value. The ambiguity can, however, be overcome by physical evidences (the spacing cannot be too large or too small).

For the $\{111\}_{MgO}//\{111\}_{Cu}$ interface obtained at $10^{-7.3}$, the interfacial distance was measured as 0.19 ± 0.01 nm. This is by 0.02 nm smaller than the spacing in copper ($d_{111} = 0.2088$ nm) perpendicular to

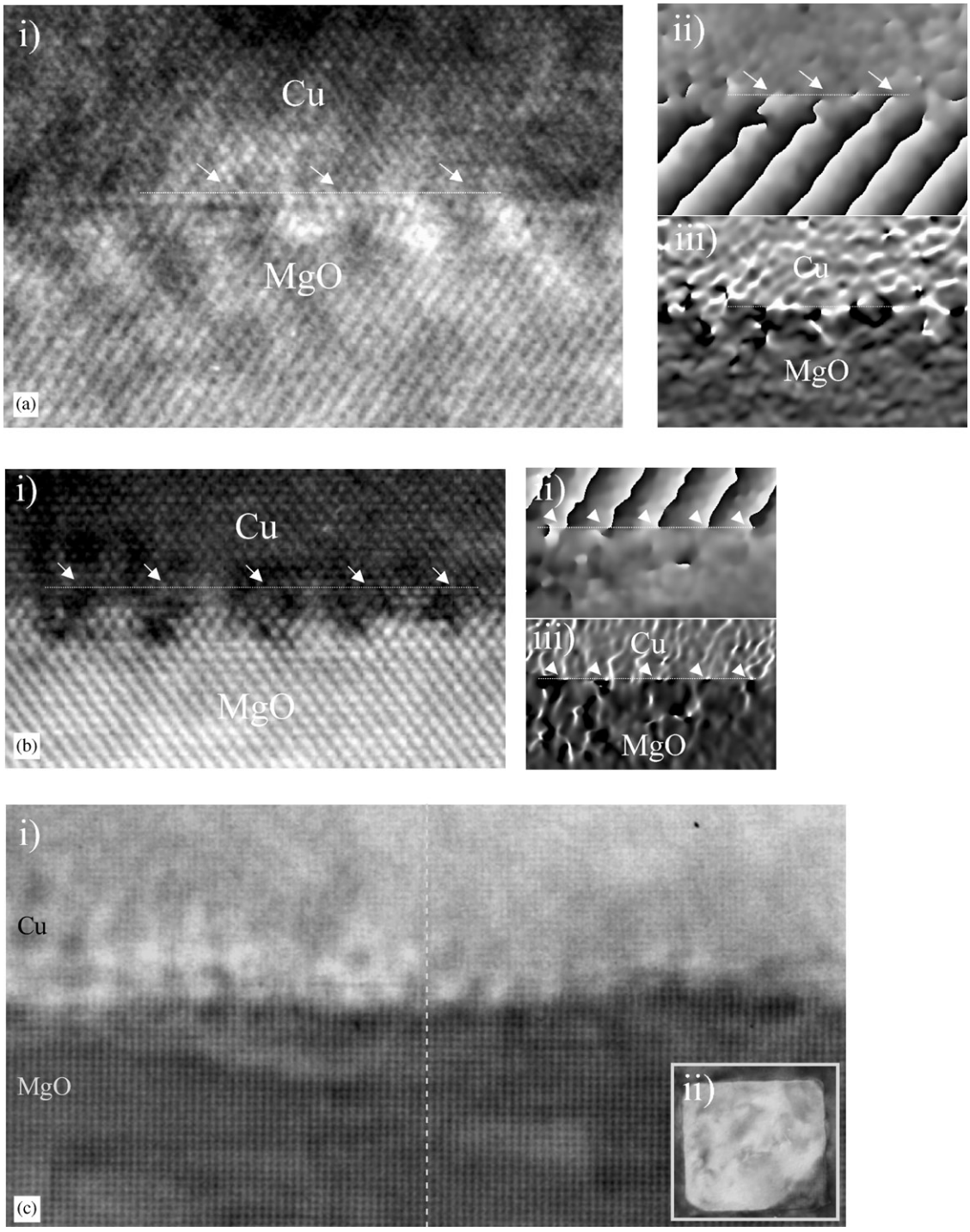

Fig. 7. HREM images of $(001)_{MgO}//(001)_{Cu}$ interfaces formed at 900°C, oxygen activity (a) 10^{-8}, (b) 10^{-12} and (c) 10^{-20} together with their maps of the local reciprocal lattice vector (gray scale proportional to $g = 1/d_{111}$) and their corresponding phase images (gray scale between 2 and 2π), arrows indicate the misfit dislocations.

the interface and much smaller than the average or that of magnesia ($d_{111} = 0.24$ nm) and can then be taken as an indication for an oxidation of copper atoms in the terminating copper plane. Copper ions are smaller in size than the metal atoms and in addition charged; therefore, they are successfully attracted by the terminating oxygen layer into this layer. As a consequence, the interfacial distance strongly diminishes. The decrease of the interplanar distance at the interface compared to the average interplane distance of both phases is taken as indication for the interfacial copper being in an oxidized state, and the average oxidation of copper at polar interfaces is expected to be the larger the more the distance is decreased.

For the $\{111\}_{MgO}//\{111\}_{Cu}$ interface at $a_{O_2} = 7 \times 10^{-14}$, see Fig. 6, the interfacial distance was 0.23 ± 0.01 nm, which is slightly smaller than the interplanar distance in magnesia and larger than the interplanar distance in copper. The value corresponds to the average of the two bulk lattice plane spacings and is the value expected for an interface without any considerable interaction. The dotted lines in Fig. 6a indicate the interfacial area, which shows lattice modifications compared to the bulk phase. The width of that zone and the periodic fluctuations in contrast along the interface indicate some important lattice relaxation. This fact can also be seen in the phase image, Fig. 6b, where instead of the well-defined dots of the dislocation core positions at high oxygen activity more extended areas of phase change can be observed.

Results on the atomic structure of $\{001\}_{MgO}//\{001\}_{Cu}$ interfaces are presented in Fig. 7 in form of the HREM images in (i), the corresponding phase image in (ii) and the gradient image in (iii). Interfaces $\{001\}_{MgO}//\{001\}_{Cu}$ equilibrated at $a_{O_2} = 10^{-7.3}$ were difficult to image because of the small size of the precipitate facet and the perturbations at the precipitate edges. Fig. 7a, however, presents an example, demonstrating that they were again smooth at an atomic scale.

At lower oxygen activity, see Fig. 7b and c, $\{001\}_{MgO}//\{001\}_{Cu}$ interfaces were not sharp at an atomic level; image contrast modulations or Moire patterns were observed, which were interpreted as sign of terracing or interface reconstruction with step heights increasing with decreasing oxygen activity. At intermediate oxygen activities, only periodic changes in contrast were observed along the interface. At $a_{O_2} = 10^{-20}$, Moire fringes in the interface area (not due to any inclination of the interface or redeposition of MgO or Cu on the sample) revealed that the interfaces no longer were atomically sharp, but terraced. We deduced from the images that typical terrace heights were 3–4 atomic planes, step lengths 7–8 columns.

For interfaces equilibrated at $a_{O_2} = 7 \times 10^{-14}$, Fig. 7b, the interfacial bond distance was determined as being 0.18 ± 0.02 nm. This value corresponds to the interplanar distance in copper, and is considered as the characteristic value of the interaction-free interface. It is smaller than the average of the two interplanar distances, but this can be related to the fact that at such an interface copper can have a preference to be situated in lock-in or on-top positions of Mg or O, creating thereby an overall relaxation, which we cannot evaluate and which is not known from atomistic calculations.

Precise measurements of the distance across the $\{001\}_{MgO}//\{001\}_{Cu}$ interface equilibrated at $a_{O_2} = 10^{-7.3}$ showed that the interfacial distance was $0.19\,\text{nm} \pm 0.01$ nm and then slightly larger than the corresponding distance in metallic copper ($d_{001} = 0.18$ nm) and definitely smaller than the distance in magnesia ($d_{001} = 0.21$ nm). This value is larger than the one found for the interaction-free interface at $a_{O_2} = 7 \times 10^{-14}$. Effectively, in case of mixed interfaces, two counteracting forces determine the interfacial distance. Oxidized copper ions are attracted by the terminating oxygen-rich layer of the oxide, and contribute with a tendency to diminish the interfacial bond distance. On the other hand, for mixed terminating oxide planes, relative oxygen excess cannot be obtained by building an excess of oxygen ions into the lattice, because there is not sufficient space available. Relative oxygen excess can only be obtained by formation of cation vacancies. Then the absence of the charge-compensating cations in the terminating plane diminishes the shielding of the oxygen anions and produces repulsive interactions between the oxygen ions. The consequence is a tendency to enlarge the bond distances perpendicular to the plane. Depending on the strength of the two counteracting forces, the interfacial distance can be either larger or smaller than the distance found for the interaction-free interface. The experimental measurement shows that the repulsive forces are stronger than the attractive ones in the geometry of the (001) interface.

3.4. Electronic structure of precipitate interfaces

For the study of the electronic structure, the following interfaces were chosen: {111} facets equilibrated at $a_{O_2} = 10^{-7.3}$, {111} and {001} facets equilibrated at $a_{O_2} = 10^{-12}$ and {001} interfacial facets equilibrated at $a_{O_2} = 10^{-20}$. {001} facets at $a_{O_2} = 10^{-7}$ and {111} facets at $a_{O_2} = 10^{-20}$ were too small in size for a proper investigation. We reinvestigated some of the interfaces, we reported on in [6,7], and obtained additional details by MSA. ELNES analysis was conducted for the characteristic ionization edges of C*u*-2*p* (Fig. 8), O-1 s (Fig. 9), M*g*-2*p* (Fig. 10). The edge intensity in the interfacial spectra was approximately half of that in the corresponding bulk spectra. For easier comparison, we normalized the intensity of all spectra.

Fig. 8a shows Cu-2*p* absorption edges of the different interfaces in normal mode, while Fig. 8b presents the corresponding normalized spatial difference (NSD) spectra. Spectra of bulk Cu, Cu_2O and CuO were added in the bottom part of Fig. 8a for easier comparison of characteristic features. The shape of the Cu-$L_{2,3}$ edge, which reflects electronic transitions from 2*p* to 3*d* levels, is very sensitive to the oxidation state of copper and the configuration of the surrounding atoms [23]. The absorption edge of metallic copper Cu(0) ($d^{10}s^1$) exhibits a typical step-like shape, while for Cu(II) in CuO (d^9s^0) most of the intensity in the near-edge region is concentrated in two narrow peaks, the so-called L_3 and L_2 white lines. Compared to copper metal, the edge threshold of CuO is shifted by 2.2 eV to lower energy.

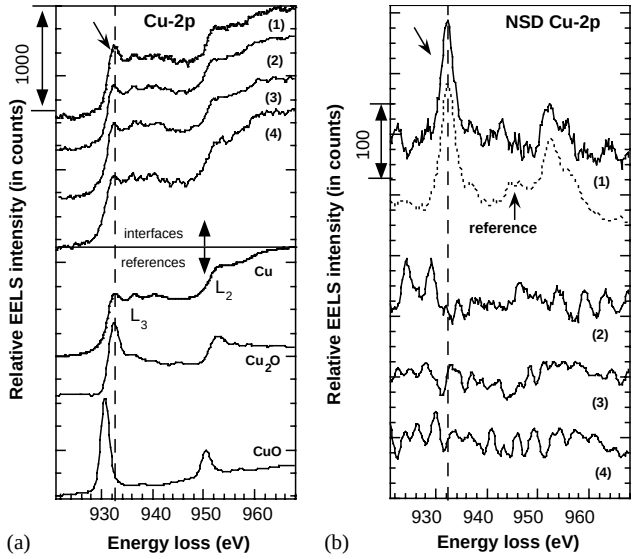

Fig. 8. (a) Cu-2*p* edge fine structure acquired in the "image-spectrum" mode: interfacial spectra of $\{111\}_{Cu}$ //$\{111\}_{MgO}$ topotaxial interfaces equilibrated at a_{O_2} =(1) 10^{-8} and (2) 10^{-12}, and $\{001\}_{Cu}$ //$\{001\}_{MgO}$ topotaxial interfaces equilibrated at a_{O_2} (3) 10^{-12} and (4) 10^{-20}. Cu_2O, CuO and metal Cu bulk reference phases are presented in the bottom part of the figure. (b) corresponding NSD spectra All spectra were normalized in intensity over an energy window of 50 eV.

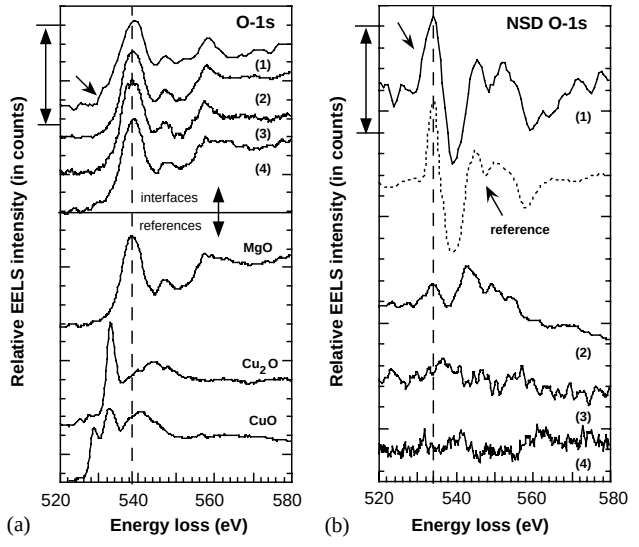

Fig. 9. (a) O-1*s* edge fine structure acquired in the "image-spectrum" mode: interfacial spectra of $\{111\}_{Cu}$//$\{111\}_{MgO}$ topotaxial interfaces equilibrated at a_{O_2} =(1) 10^{-8} and (2) 10^{-12}, and $\{001\}_{Cu}$ //$\{001\}_{MgO}$ topotaxial interfaces equilibrated at a_{O_2} (3) 10^{-12} and (4) 10^{-20}. Cu_2O, CuO and MgO bulk reference phases are presented in the bottom part of the figure. (b) Corresponding NSD spectra. All spectra were normalized in intensity over an energy window of 50 eV.

The Cu_2O spectrum exhibits an edge shape as metallic copper (step-like behavior), which is superposed by Cu-$L_{2,3}$ white lines of much lower intensity than those of CuO. No chemical shift in the absorption threshold compared to Cu(0) can be experimentally determined by EELS (with an energy dispersion of 0.2 eV/ch).

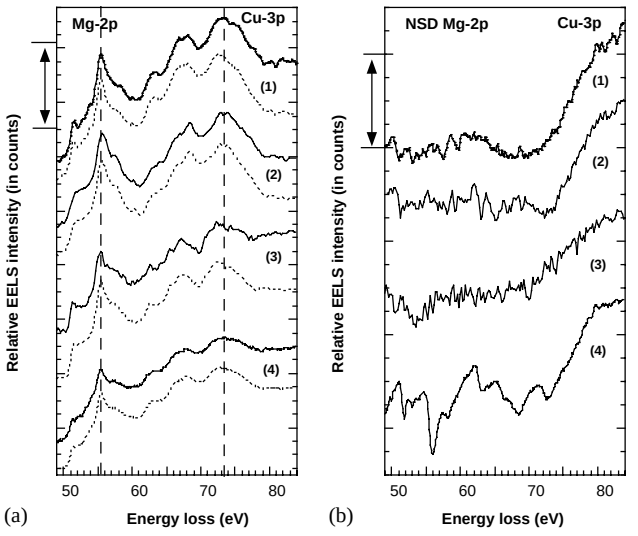

Fig. 10. (a) Mg-2*p* edge fine structure acquired in the "image-spectrum" mode: interfacial spectra of $\{111\}_{Cu}$//$\{111\}_{MgO}$ topotaxial interfaces equilibrated at p_{O2} (1) 10^{-8} and (2) 10^{-12}, and of $\{001\}_{Cu}$ // $\{001\}_{MgO}$ topotaxial interfaces equilibrated at a_{O_2} (3) 10^{-12} and (4) 10^{-20}. Corresponding bulk spectra are represented in dotted lines. (b) corresponding NSD. All spectra were normalized in intensity over an energy window of 25 eV.

Spectra (1), (2), (3) and (4) in Fig. 8a were acquired for the interfacial facets {111} equilibrated at $a_{O_2} = 10^{-8}$, {111} at $a_{O_2} = 10^{-12}$, {100} at $a_{O_2} = 10^{-12}$ and {100} at $a_{O_2} = 10^{-20}$ respectively. For $a_{O_2} = 10^{-7.3}$, a considerable increase in L_3 white-line intensity was observed (the dotted line in Fig. 8a indicates the corresponding energy)). No such increase was observed for the two lower oxygen activities. For the lower oxygen activities, it was noted that the two small peaks following L_3 at 936 and 938 eV diminished or even disappeared at the interface. These peaks are characteristics for metallic fcc copper. This finding confirms the HREM observation of a perturbation of the crystalline copper structure close to the interface for those lower oxygen activities. Depending on the exact location at the interface, the effect was more or less pronounced, however, in average, it was more important at lower oxygen activity.

The most interesting observation, however, was the increase in L_3 intensity at high oxygen activity. It is explained by an hybridization of Cu-3*d* and O-2*p* states. Since no chemical shift was observed, the interfacial electronic structure must be close to that of bulk Cu_2O, even though the arrangement of neighbor atoms is different at the metal–oxide interface.

Fig. 8b shows the NSD spectra corresponding to spectra (1), (2), (3) and (4) of Fig. 8a. It shall be recalled that the amplitude of the NSD spectrum directly depends on the difference in the differential inelastic cross sections of the corresponding edges [7]. In Fig. 8b, the linear combination of spectra of bulk copper and bulk Cu_2O was added as dotted lines. The fit between

this linear combination and the interfacial NSD at $a_{O_2} = 10^{-7}$ is sufficiently good to suggest that the interfacial electronic structure must be very close to that of cuprite. At the other oxygen activities, no such similarity was found. Therefore, this type of hybridization across the interface must be weaker or not present at all. The intensities of the residual signal in the corresponding NSD spectra were in the order of the noise and suggest that, at the interface, no particular electronic structure was observed at lower oxygen activities.

Fig. 9 shows O-1*s* edges of interfacial areas having been also analyzed for Fig. 8. Spectra of bulk MgO, Cu_2O and CuO were added in the bottom part of Fig. 9a. Fig. 9a shows spectra in the normal mode, Fig. 9b the corresponding NSD spectra. For further comparison, the NSD spectrum of a combination of bulk MgO and bulk Cu_2O is depicted as dotted line in Fig. 9b.

Both, normal mode and NSD spectra, showed that the O-1*s* edge was strongly modified at high oxygen activity ($a_{O_2} = 10^{-7}$). Edge enlargement and presence of a low-energy shoulder were the typical characteristics. They are linked to the hybridization of Cu-3*d* and O-2*p* states, which was already observed in the Cu spectra for the same experimental condition.

The NSD spectrum (2) corresponding to the {111} interface obtained at $a_{O_2} = 10^{-13}$ showed a weak residual signal, which was similar to that observed for $a_{O_2} = 10^{-7}$. This indicates that hybridization of the states still occurred at lowered oxygen activity, but that the hybrid state density was much lower. This weak interaction was not observed in the corresponding Cu-edge, probably because the cross section for inelastic scattering is larger for the O-K edge than for the Cu-L edge and (with the same detector) the detection sensibility for this edge was higher.

For {001} interfaces at $a_{O_2} = 10^{-13}$ and 10^{-20} only residual noise was observed. Therefore, it was concluded that the electronic structure at these interfaces had to be the one of bulk MgO.

Fig. 10 represents results on the Mg-2*p* edge. Being close to the plasmon region, its exploration was difficult. The spectra in Fig. 10a were obtained after deconvolution, Fig. 10b presents the corresponding NSD spectra. Representative spectra for interfaces equilibrated at $a_{O_2} = 10^{-8}$ and 10^{-13} showed no significant changes compared to bulk MgO, neither in the normal mode, nor in the NSD mode. The Cu-M edge threshold is located at 74 eV, therefore, the interfacial Mg-2*p* edge was partially superposed by the tail of the Cu-M edge and edge details could only be explored for energies below 74 eV. For {001} interfaces obtained at 10^{-20}, the NSD showed a residual spectrum, which did not fit spectra of metallic Mg or Cu_2Mg alloy. While no electronic structure calculations of different interfacial configurations or better fitting bulk references are available, it is suggested, that this residual spectrum indicates some interaction between copper and magnesium, the character of which has still to be identified in the future.

4. Discussion

Continuum thermodynamics predict Gibbs' adsorption [36] of excess oxygen and magnesium to non-reactive metal–oxide interfaces at high and low oxygen activity, respectively. The adsorption isotherms depend strongly on the adsorption energy of oxygen and magnesium to the interface, their magnitude being strongly linked to the energy of the new-formed bonds across the interface and the interface crystallography. The Gibbs' adsorption model has been adapted to the problem of interfacial chemistry at metal–oxide by one of the authors [21,22] and applied to Cu–MgO interfaces. Details on the general model and the computation of the adsorption isotherms are described in Ref. [22]. Three general types of interfaces were predicted, each of it associated with an oxygen activity domain:

- Oxygen-impoverished interfaces in a low oxygen activity domain with relative oxygen deficiency being achieved either by adsorption of excess magnesium to polar magnesium-terminated planes or by desorption of oxygen from mixed planes.
- Stoichiometric interfaces in an intermediate oxygen activity range with fully occupied planes for mixed interfaces and half occupied planes for polar interfaces.
- Oxygen-enriched interfaces at high oxygen activity with relative oxygen excess being established either by adsorption of excess oxygen to the terminating mixed polar planes or by desorption of magnesium from mixed planes.

The limits of the three oxygen activity domains were shown to considerably depend on the magnitude of the adsorption energies used in the model. Backhaus [22] proposed to use in a first-order approach bulk enthalpy values and an entropy term derived from statistical considerations. More appropriate approximations were suggested with energies including in addition strain energy contributions in the interfacial slab due to volume changes accompanying the different adsorption/desorption reactions. Fig. 11 presents occupancy curves of {001} and oxygen-terminated {111} and magnesium terminated {111} MgO–Cu interfaces obtained with different approximations: (I) adsorption energies were approximated by the bulk formation enthalpies of Cu_2O and Cu_2Mg, (II) adsorption energies were approximated by the bulk formation enthalpies of Cu_2O and Cu_2Mg and a configurational adsorption entropy, (III) volume changes upon adsorption were

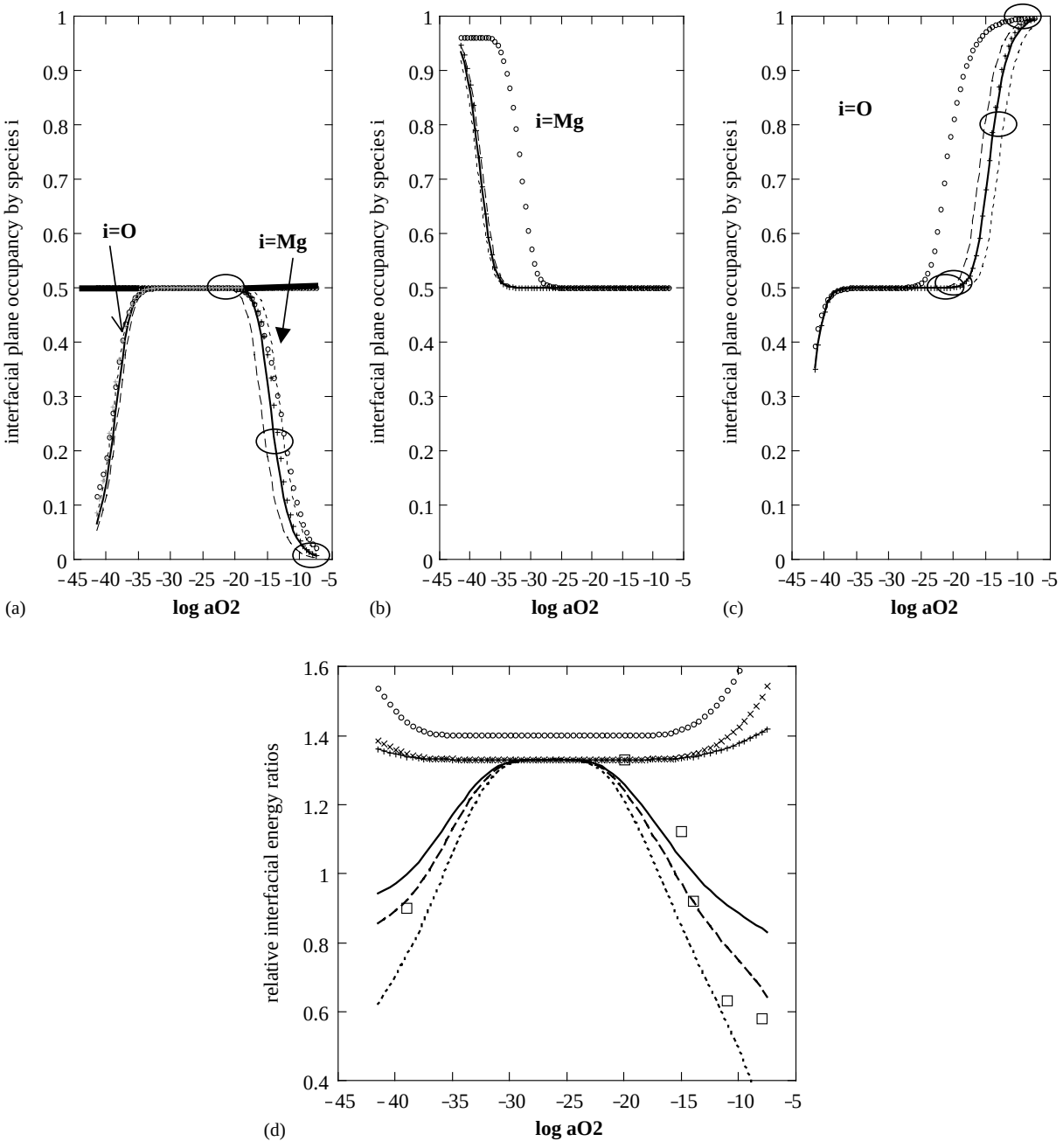

Fig. 11. Occupancies of the terminating oxide plane as function of oxygen activity for (a) mixed $(001)_{MgO}//(001)_{Cu}$, (b) polar O-terminated $(111\text{-}O)_{MgO}//(111)_{Cu}$ and (c) polar Mg-terminated $(111\text{-}Mg)_{MgO}//(111)_{Cu}$ interfaces.The curves represented computed model predictions for different values of the adsorption energies; the continuous line corresponds to the volume formation enthalpy of the corresponding bulk phases Cu_2O and Cu_2Mg, the dotted line to 90% of these values, the dashed line to 110% of these values, circles represent a computation, which includes in addition to the enthalpies a reaction volume-related strain energy term and the crosses show the shift of the adsorption behavior, when not only the enthalpy, but also a configurational adsorption entropy is considered. The large open dots show our experimental ELNES results. (d) Relative ratios of $(111\text{-}O)_{MgO}//(111)_{Cu}$ and $(001)_{MgO}//(001)_{Cu}$ free interfacial energies $\gamma_{111}/\gamma_{001}$ and $(111\text{-}O)_{MgO}//(111)_{Cu}$ and $(001)_{MgO}//(001)_{Cu}$ free interfacial energies $\gamma_{011}/\gamma_{001}$ as function of the oxygen activity at 900°C. The curve composed of small circles shows model predictions for $\gamma_{011}/\gamma_{001}$; all other curves show model predictions for $\gamma_{111}/\gamma_{001}$. Crosses ($\gamma_{001} = 1200$ J/m^2) and inclined crosses ($\gamma^{001} = 1600$ J/m^2) are obtained when using the formation enthalpies of the corresponding bulk phases Cu_2O and Cu_2Mg as adsorption energies, continuous ($\gamma_{001} = 2000$ J/m^2) , dashed ($\gamma_{001} = 1600$ J/m^2) and dotted ($\gamma_{001} = 1200$ J/m^2) lines are obtained when including in addition to the bulk enthalpy values a strain energy that is related to the volume changes upon adsorption. The large squares show our experimental results of precipitate Wulff shapes.

taken into account and approximated in the form of an adsorption strain energy, which was deduced on the basis of the Schottky pair formation energy in MgO, (IV) and (V) correspond to approximation (I) under use of 10% smaller and larger enthalpy values, respectively.

It shall be underlined that the general trends in the adsorption isotherms are the same for all assumptions. The different input energies change the quantitative adsorption at given oxygen chemical potential. It is evident that the onset of adsorption or desorption strongly depends on the adsorption enthalpy. While the branches of the adsorption curves are only shifted on the x-axis for different enthalpy values, the consideration of a concentration-dependent adsorption strain energy induces changes in the slope of the adsorption branches. It can be further seen that the changes in the configurational entropy upon adsorption introduce only minor changes, which can be neglected in the computation. It is difficult to evaluate the strain energy, because reaction-related stresses may partly relax. In the computation, we used a maximum possible value for the strain energy without any stress relaxation. Ab inito calculations may provide better approximations for the adsorption energy, but for the considered system such values are not available.

On the other hand, our experimental results can be used to determine the Gibbs' adsorption energies through their best fit with a theoretical curve for a certain set of input data. For this reason, ELNES results were added to Fig. 11 in form of circular symbols, which shall not to be understood as precise data points, but trends. Oxide bonding across the interface reflects the presence of oxygen excess at the interface, because formally every oxide bond established between copper and oxide corresponds to an unit of Cu_2O, which formed under oxidation of metallic copper by an excess atom of oxygen. Therefore, we can quantify the ELNES results in terms of excess oxygen. For the $\{111\}_{Cu}//\{111\}_{MgO}$ and $\{001\}_{Cu}//\{001\}_{MgO}$ interfaces equilibrated at $a_{O_2} = 10^{-7.3}$, the interfacial signal intensity was quantified for the given geometry, beam broadening etc., see Ref. [7], yielding oxygen excess concentrations of 0.55 and 0.4 times the total number of oxygen sites on the corresponding atomic planes, respectively. The much smaller intensity of the interfacial hybrid signal at oxygen activity 10^{-13} makes an exact quantification difficult. For all lower oxygen activity, no modification in interfacial electronic states was observed, indicating that, at the interface, stoichiometric magnesia and copper coexist.

HREM results on the interfacial bond distance can be interpreted in a similar semi-quantitative manner: At the highest oxygen activity, an important decrease in interfacial bond distance was observed for {111} facets, which was related to oxidation of interfacial copper and presence of excess oxygen. For {001} facets, in contrast, an increase in interfacial bond distance was observed, which was also related to the presence of oxidized copper, but in this case combined with a deficiency of magnesium in the mixed plane. With decreasing oxygen chemical potential, interfacial bond distances approached an intermediate value between bulk copper and bulk magnesia, showing then that the bulk phases coexisted without major changes in the atomic and electronic structure. From these observations we can deduce the presence of excess oxygen at the interface in the high oxygen activity domain and tell that the excess concentrations diminish with decreasing oxygen activity, but we cannot quantify the concentrations.

In Fig. 11d, the ratio of $(111\text{-O})_{MgO}//(111)_{Cu}$ and $(001)_{MgO}//(001)_{Cu}$ free interfacial energies $\gamma_{111}/\gamma_{001}$ as function of the oxygen activity at 900°C. Different absolute values of the absolute energy of the $(001)_{MgO}//(001)_{Cu}$ interface have been considered, covering the possible range of its value from $\gamma_{001} = 1200\text{–}2000\ J/m^2$ indicated by various literature results ranging from ab initio calculations to wetting angle measurements. For the adsorption energies, two different assumptions are compared. In a first set of calculations, the adsorption energy was approximated by the formation enthalpies of the corresponding bulk phases Cu_2O and Cu_2Mg. For a second set of calculations, the adsorption energy was approximated by the corresponding bulk formation enthalpies and a strain energy contribution that is related to the volume changes upon adsorption. The strain energy was computed by considering the missing or excess lattice molecules formed upon adsorption and associating their energy to the energy of formation of associated Schottky defects in magnesia.

A curve for the ratio of $(111\text{-O})_{MgO}//(111)_{Cu}$ and $(001)_{MgO}//(001)_{Cu}$ free interfacial energies $\gamma_{011}/\gamma_{001}$ as function of the oxygen activity at 900°C is added. It was computed with the bulk formation enthalpy values as adsorption energy. This curves show that upon adsorption, mixed planes with lower atom density than the (001) plane increase in their relative energy and become less stable. As a consequence, such precipitate facets are expected to diminish in size upon adsorption.

The large open square dots in the figure show the experimental results for $\gamma_{111}/\gamma_{001}$ we obtained from Wulff shapes of MgO precipitates in Cu. They are not well fitted by using the simple bulk phase formation enthalpy values as adsorption energy. A difference in adsorption behavior between polar and mixed interfaces in the model is necessary to fit the experimental results. This difference can be introduced through the larger strain energy contribution for the polar interfaces. The curves obtained for unrelaxed adsorption stresses effectively fit the experimental results. The experimental values could are best fitted if we consider only 80% of the volume changes as un-relaxed, while 20% of the stress do relax.

From our experimental observations of the atomic and electronic structure of the polar and mixed interfaces at different oxygen activities, we can derive a simple model for the unrelaxed atomic structures of the interfaces in the different oxygen activity domains.

In Figs. 12a–c and 13 a–c, those structures are schematically depicted. The adsorption-free interfaces are shown in Figs. 12b and 13b. While the mixed MgO–Cu interface is made of a (001) magnesia and a (001) copper plane with their regular bulk occupancies, the polar interface is composed of a regular (111) copper plane and an only half occupied (111-O) oxygen plane. The occupancy half corresponds to the electroneutrality of the magnesia half-crystal. At high oxygen activity, a relative oxygen excess is established by adsorption of excess oxygen to the structural vacancies of the half-occupied (111-O) terminating oxide plane in case of the polar interface or by desorption of magnesium from the regular terminating (001) oxide plane. At the highest oxygen activity, the terminating (111-O) oxide plane is completely occupied, see Fig. 12a, providing then an atomically flat interface with minimal relaxation in the interfacial area. Mixed interfaces at the same highest oxygen activity should show a high number of missing cations, see Fig. 13a. For not fully occupied oxygen terminating planes, more or less important structural relaxation is expected for polar interfaces, see Fig. 12b, which conducts to important perturbations of the copper lattice in proximity of the interface. At very low oxygen activities, according to our modeling for $a_{O_2} < 10^{-35}$ at 900°C, relative oxygen deficiency establishes at the interface. For polar interfaces, the terminating oxide plane will then be made by magnesium and will be more than half occupied, see Fig. 12c. Mixed interfaces become magnesium-rich by desorption of oxygen from the terminating mixed oxide plane, creating thereby

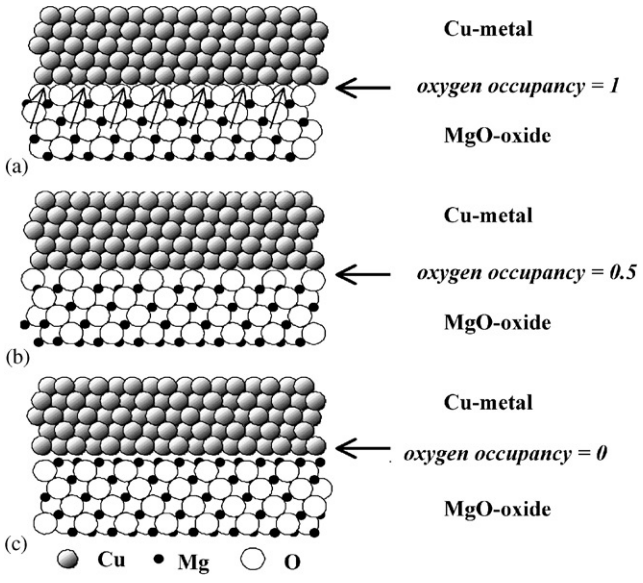

Fig. 12. Schematic presentation of the unrelaxed structure of the polar $\{111\}_{MgO}//\{111\}_{Cu}$ MgO–Cu interface in the different oxygen potential domains. interface (a) with oxygen excess in the high oxygen activity range, (b) in its adsorption-free state in the intermediate oxygen activity range and (c) with relative magnesium excess in the low oxygen activity range. Possible atomic relaxation is indicated by arrows.

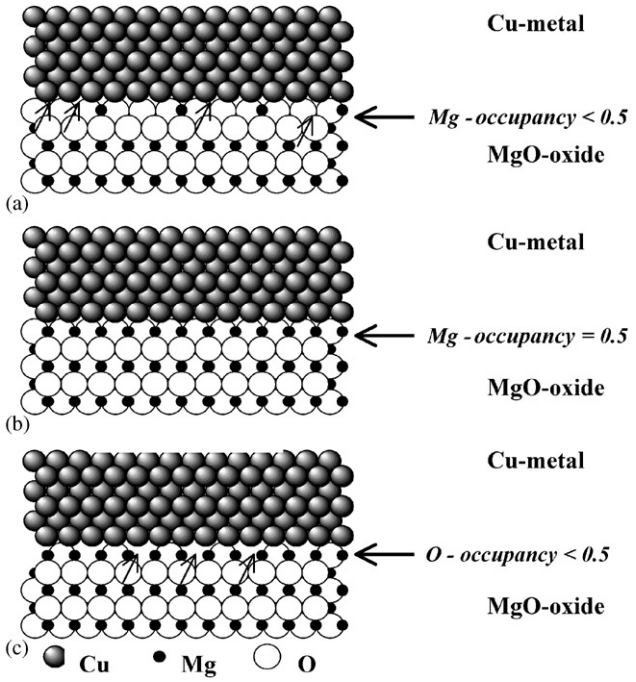

Fig. 13. Schematic presentation of the unrelaxed structure of the mixed $\{001\}_{MgO}//\{001\}_{Cu}$ MgO–Cu interface in the different oxygen potential domains: (a) with oxygen excess in the high oxygen activity range. (b) in its adsorption-free state in the intermediate oxygen activity range and (c) with relative magnesium excess in the low oxygen activity range. Possible atomic relaxation is indicated by arrows.

oxygen vacancies, which induce major structural relaxation in the adjacent copper lattice, Fig. 13c. In these schematic considerations, it is not considered that oxygen vacancies in the oxide plane may be occupied by Cu atoms (an energy advantage was calculated for occupation of surface vacancies of magnesia by metal atoms), thereby producing an interface, which is no longer atomically sharp. Such substituting Cu atoms may order in the interfacial plane and thereby produce terracing. However, from image analysis and experimental observations we are not able to state, that this is the only interpretation of the Moiré contrasts we observed at interfaces equilibrated at lower oxygen activity.

In Fig. 12, relaxation of the atomic structure is indicated by arrows, charge transfer between copper atoms and oxygen or copper atoms and magnesium is indicated by black and white dotted lines, respectively.

Figs. 11–13 conclude all our knowledge of the atomic and electronic structure of MgO–Cu interfaces, together with their relative energies and stability domains and, in addition, provide a summary of our experimental results.

5. Conclusions

In (Cu,Mg) alloys oxidized at 900°C and different oxygen chemical potential, two kinds of MgO precipi-

tates were found, cubo-octahedral precipitates and large fractal agglomerates. It is suggested that the two types of precipitates form by different mechanisms, at high and low oxygen content, respectively. Only the small-sized cubo-octahedral precipitates achieve their equilibrium shape.

Their morphology varies systematically with increasing oxygen activity from cubic to octahedral shape. A combined study of the atomic and electronic structure of the different precipitate interfaces obtained at different oxygen chemical potential showed that the Cu–MgO interface is not unique, but univariant and that local interfacial composition and interfacial bonding depend on the oxygen chemical potential. Changes in interfacial chemistry produce a dependency of the relative interfacial energy on the oxygen chemical potential, which generates the observed evolution in morphology.

Even though our study was conducted for a very simple model system, it is of general validity and can be easily extrapolated for other transition metal–oxide interfaces.

Acknowledgments

The authors thank P. Ochin, A. Dezellus and P. Plaindoux for processing the (Cu,Mg) alloys, J.C. Rouchaud for the ICP analysis, J.Devaud for help with the HREM studies, S. Laurent for preliminary investigations and S. Hagège, C. Colliex and T. Manoubi for discussion on the subject.

References

[1] H. Schmalzried, Chemical Kinetics of Solids, VCH, Weinheim, 1995.
[2] J. Maier, Festkoerper-Fehler und Funktion, TeubnerVerlag, Leipzig, 2000.
[3] H. Schmalzried, M. Backhaus-Ricoult, Progr. Solid State Chem. 22 (1993) 1–57.
[4] C. Wagner, J. electrochem. Soc. 103 (1956) 571–580.
[5] J. Gegner, G. Horz, R. Kirchheim, Interface Sci. 5 (4) (1997) 231–243.
[6] S. Laurent, D. Imhoff, C. Colliex, M. Backhaus-Ricoult, Variation of interfacial structure and chemistry of topotactic {111}MgO–Cu interfaces with the oxygen chemical potential, in Intergranular and Interphase Boundaries in Materials, Iib98. 1999, Transtec Publications Ltd, Zurich-Uetikon, pp. 325–328
[7] D. Imhoff, S. Laurent, C. Colliex, M. Backhaus-Ricoult, Eur Phys. J. Appli. Phys. 5 (1) (1999) 9–18.
[8] M. Backhaus-Ricoult, S. Laurent, J. Devaud, M. Hÿtch, D. Imhoff, S. Hagège, J. Phys. IV 9 (P4) (1999) 13.
[9] M. Backhaus-Ricoult, unpublished results.
[10] M. Backhaus-Ricoult, L. Samet, M. Thomas, M.-F. Trichet, D. Imhoff, Acta Mat. 50 (2002) 4191–4204.
[11] E. Pippel, J. Woltersdorf, J. Gegner, et al., Acta Mater. 48 (10) (2000) 2571–2578.
[12] M. Backhaus-Ricoult, M.-F. Trichet, Z. Metallkunde, in press.
[13] M. Backhaus-Ricoult, S. Laurent, Anisotropy and oxygen activity dependency of the liquid or solid metal-oxide interfacial free energy: case study on MgO–Cu, in: intergranular and interphase boundaries in materials, iib98. Transtec Publications Ltd, Zurich-Uetikon. 1999, p. 173-176.
[14] M. Backhaus-Ricoult, Nova Acta Leopoldina NF38 (2000) 127–154.
[15] M. Backhaus-Ricoult, Acta Mater. 49 (2001) 1747–1758.
[16] E. Saiz, A.T. Tomsia, R.M. Cannon, In: Ceramic Microstructure: Control at an Atomic Level, A.P. Tomsia, A.M. Glaeser (Eds.), Plenum Press, New York, 1996, p. 65
[17] D. Chatain, F. Chabert, V. Ghetta, J. Fouletier, J. Am. Ceram. Soc. 77 (1994) 197.
[18] I.G. Batyrev, A. Alavi, M.W. Finnis, Phys. Rev. B 62 (2000) 4698.
[19] M.W. Finnis, J. Phys., Condens. Matter 8 (1996) 5811.
[20] W. Zhang, J.R. Smith, Phys. Rev. B 24 (2000) 116883.
[21] M. Backhaus-Ricoult, Acta Mater. 48 (18-19) (2000) 4365–4374.
[22] M. Backhaus-Ricoult, Philos Mag. A 81 (2001) 1759–1787.
[23] F.N. Rhines, Trans. AIME 137 (1940) 146–190.
[24] L. Charrin, A. Combe, J. Cabane, Oxid. Metals 37 (1992) 65–80.
[25] C. Wagner, Corrosion Sci. 8 (1968) 889–893.
[26] H. Jang, D.N. Seidmann, K.L. Merkle, Interface Sci. 1 (1993) 61.
[27] D.A. Muller, D.A. Shashkov, R. Benedek, L.H. Yang, J. Silcox, D.N. Seidmann, Phys. Rev. Lett. 80 (1998) 4741.
[28] M.J. Hytch, E. Snoek, R. Kilaas, Ultramicroscopy 74 (1998) 131–146.
[29] C.T. Colliex, M. Leféve, E. Mory, C. Gu, D. Bouchet, C. Jeanguillame, Mikrochim. 71 (1994) 114–115.
[30] N. Bonnet, J. Microsc.-Oxford 190 (1998) 2–18.
[31] N. Bonnet, N. Brun, C. Colliex, Ultramicroscopy 77 (1999) 97–112.
[32] G. Duscher, Conf. proceedings iib.
[33] E. Snoek, B. Warrot, H. Ardhuin, A. Rocher, M.J. Casanove, R. Kilaas, M.J. Hÿtch, Thin Solid Films 319 (1998) 157–162.
[34] M.J. Hÿtch, T. Plaman, Ultramicroscopy 87 (2001) 199–201.
[35] A. Pojani, F. Finocchi, J. Goniakowski, C. Noguéra, Surf. Sci. 387 (1997) 354.
[36] J.W. Gibbs, Scientific Papers (1878), Dover Publ, New York, (1961).